Simulation of viscoelastic squeeze flows for adhesive joining applications

Journal of Non-Newtonian Fluid Mechanics 300 (2022) 104722

Contents lists available at ScienceDirect

Journal of Non-Newtonian Fluid Mechanics

journal homepage: www.elsevier.com/locate/jnnfm

Simulation of viscoelastic squeeze flows for adhesive joining applications

Simon Ingelsten [a,b,*], Andreas Mark [a], Roland Kádár [b], Fredrik Edelvik [a]

[a] Fraunhofer-Chalmers Research Centre for Industrial Mathematics, Gothenburg, 412 88, Sweden
[b] Division of Engineering Material, Department of Industrial and Materials Science, Gothenburg, 412 96, Sweden

ARTICLE INFO

Keywords:
Non-Newtonian flow
Computational fluid dynamics
Squeeze flow
Volume of fluid
Immersed boundary method
Assembly simulation
Adhesive joining

ABSTRACT

A backwards-tracking Lagrangian–Eulerian method is used to simulate planar viscoelastic squeeze flow. The momentum and continuity equations are discretized with the finite volume method and implicit immersed boundary conditions are used to describe objects in the domain. The viscoelastic squeeze flow, which involves moving solid geometry as well as free surface flow, is chosen for its relevance in industrial applications, such as adhesive parts assembly and hemming. The main objectives are to validate the numerical method for such flows and to outline the grid resolution dependence of important flow quantities. The main part of the study is performed with the Oldroyd-B model, for which the grid dependence is assessed over a wide range of Weissenberg numbers. An important conclusion is that the load exerted on the solids can be predicted with reasonable accuracy using a relatively coarse grid. Furthermore, the results are found to be in excellent agreement with theoretical predictions as well as in qualitative resemblance with numerical results from the literature. The effects of different viscoelastic properties are further investigated using the PTT model, revealing a strong influence of shear-thinning for moderate Weissenberg numbers. Finally, a reverse squeeze flow is simulated, highlighting important aspects in the context of adhesive joining applications.

1. Introduction

Viscoelastic fluids appear in various industrial processes, including polymer processing, additive manufacturing, seam sealing and adhesive joining applications such as parts assembly and hemming. For adhesive joining applications, the ability to test different joining concepts, material combinations and geometry variations through numerical simulations is a powerful tool for the development process. Robust and efficient numerical methods are therefore needed, which predict the flow of the adhesive as well as the loads exerted on the product and the production equipment. The numerical models typically need to involve viscoelastic free surface flow which is driven by moving solids.

A common approach to viscoelastic flow simulation is to solve equations in the Eulerian frame of reference. Many examples may be found in the literature, for example with the finite volume method (FVM) [1–3] or the finite element method (FEM) [4,5]. The Eulerian frame is well-suited for diffusion-dominated problems, e.g. viscous flow or heat and mass transfer. However, viscoelastic constitutive equations are typically hyperbolic and lack physical diffusion. Therefore, intuitively the Lagrangian frame of reference provides a natural description for the viscoelastic stress transport. Consequently, Lagrangian or semi-Lagrangian methods constitute appealing alternatives to fully Eulerian methods. Examples of the Lagrangian approach include the Lagrangian FEM method by Rasmussen and Hassager [6] and the split Lagrangian–Eulerian FEM method by Harlen et al. [7]. In both methods, the computational mesh was deformed over the course of the simulation and re-meshing was thus necessary. Another example is the Lagrangian particle method (LPM) by Halin et al. [8]. The viscoelastic constitutive equation was solved for massless particles in the flow and polynomial reconstruction was used to calculate the viscoelastic stress terms in the FEM used to solve the momentum equations. This imposed a lower limit on the number of particles per element for the simulations not to fail, and a fairly large number of particles was required for stable simulations. The method was further developed into the more adaptive ALPM by Gallez et al. [9] and the backward-tracking BLPM by Wapperom et al. [10].

An important component in adhesive joining applications is non-Newtonian squeeze flow. Phan Thien and coworkers studied squeezing flows of viscoelastic fluids as early as in the 1980's, motivated by its implications for bearing lubrication in unsteady load conditions as well as for measurement applications [11–13]. They developed a theoretical framework, leading up to a set of partial differential equations which could be solved numerically. Moreover, asymptotic solutions for the load exerted on the solid geometries were derived in the limits of small and large Weissenberg numbers, respectively. Debbaut et al. [14]

* Corresponding author at: Fraunhofer-Chalmers Research Centre for Industrial Mathematics, Gothenburg, 412 88, Sweden.
E-mail address: simon.ingelsten@fcc.chalmers.se (S. Ingelsten).

https://doi.org/10.1016/j.jnnfm.2021.104722
Received 5 July 2021; Received in revised form 26 November 2021; Accepted 9 December 2021
Available online 1 January 2022

performed axisymmetric simulations in the finite element-based flow solver Polyflow [15] to investigate viscoelastic and non-isothermal effects in squeeze flows, which are of interest e.g. for compression molding applications. Shafahi and Ashrafi [16] later simulated the flow of a shear-thinning fluid in a similar configuration using a finite volume method with a moving mesh scheme. Other numerical studies on squeeze flows in general include e.g. Duwairi et al. [17] and Kaushik et al. [18]. The former simulated non-isothermal flow of a Newtonian fluid subject to simultaneous squeeze and extrusion in a one-dimensional configuration. The latter more recently used a similar configuration for the isothermal flow of an Oldroyd-B fluid. An extensive summary on squeeze-flows was presented by Engmann et al. [19].

In our previous research, a Lagrangian–Eulerian method for simulation of viscoelastic has been developed [20,21]. The viscoelastic constitutive equation is solved in Lagrangian fluid elements and the stresses are coupled to the momentum equation through unstructured interpolation with radial basis functions. An improved formulation of the method was later presented, based on backwards-tracking [22]. In the new formulation, the storage locations for the viscoelastic stresses are explicitly chosen. Consequently, the unstructured interpolation is eliminated and the total number of Lagrangian nodes is reduced. In the same study, the method was also extended to simulation of viscoelastic free surface flow with the volume of fluid (VOF) method. The method is implemented in the software IPS IBOFlow® [23], a finite volume-based flow solver developed at the Fraunhofer-Chalmers Research Centre for Industrial Mathematics in Gothenburg, Sweden. In addition to viscoelastic fluid flow, the solver has been employed for simulation of free surface flow of shear thinning fluids with applications for automotive seam sealing [24,25], adhesive application [26] and 3D-bioprinting [27], as well as for fluid–structure interaction [28] and conjugated heat transfer [29–31].

In the current study, the backwards-tracking Lagrangian–Eulerian method is used for viscoelastic squeeze flow with free surfaces and moving solid geometry. The aim of the study is to validate the numerical method for this type of flow, as well as to investigate the dependency on grid resolution for prediction of certain quantities. A quantity of particular interest is the load exerted by the viscoelastic fluid on the solid objects. This property is important e.g. as the forces on the product geometry or the production equipment during an adhesive joining operation. In addition, accurate prediction of the load is crucial for fluid–structure interaction (FSI) applications. Such an example is hemming, for which it is necessary to include solid deformations in the numerical model. Within the context of adhesive joining in general, and hemming in particular, a study of the corresponding reverse squeeze flow is also presented.

The rest of the paper is structured as follows. First the governing equations are stated, followed by a presentation of the numerical method. In the results section, a grid dependence study for a wide range of Weissenberg numbers is presented for the viscoelastic squeeze flow considered. The load exerted on the upper plate is then compared for different viscoelastic fluids for the considered flows. Finally, the conclusions are stated and an outlook is given.

2. Governing equations

The viscoelastic fluid flow is described by the incompressible momentum and continuity equations

$$\rho\left(\frac{\partial \mathbf{u}}{\partial t}+\mathbf{u}\cdot\nabla\mathbf{u}\right)=-\nabla p+\nabla\cdot(2\eta_s\mathbf{S}+\boldsymbol{\tau})+\mathbf{f}, \tag{1}$$

$$\nabla\cdot\mathbf{u}=0, \tag{2}$$

where ρ is density, $\mathbf{u}$ velocity, p pressure, η_s solvent viscosity, i.e. the Newtonian contribution to viscosity, $\mathbf{S}=\frac{1}{2}(\nabla\mathbf{u}+(\nabla\mathbf{u})^T)$ the strain rate tensor, $\boldsymbol{\tau}$ viscoelastic stress and $\mathbf{f}$ a body force. The viscoelastic stress $\boldsymbol{\tau}$ is described by a constitutive equation of the form

$$\lambda\overset{\triangledown}{\boldsymbol{\tau}}+F(\boldsymbol{\tau})\boldsymbol{\tau}=2\eta_p\mathbf{S}, \tag{3}$$

where λ is the relaxation time, η_p polymeric viscosity and F a scalar-valued function which depends on which constitutive model is used. $\overset{\triangledown}{\boldsymbol{\tau}}$ is the upper-convected derivative of $\boldsymbol{\tau}$ and expands to

$$\overset{\triangledown}{\boldsymbol{\tau}}=\frac{D\boldsymbol{\tau}}{Dt}-(\nabla\mathbf{u})^T\cdot\boldsymbol{\tau}-\boldsymbol{\tau}\cdot\nabla\mathbf{u}, \tag{4}$$

where $\frac{D\boldsymbol{\tau}}{Dt}$ is the Lagrangian time derivative of $\boldsymbol{\tau}$. While (3) and (4) do not represent all viscoelastic constitutive models, they cover those considered in the current work. These are the Oldroyd-B model [32]

$$F(\boldsymbol{\tau})\equiv 1, \tag{5}$$

the linear-form PTT model [33]

$$F(\boldsymbol{\tau})=\left(1+\frac{\varepsilon\lambda}{\eta_p}\mathrm{Tr}\,(\boldsymbol{\tau})\right), \tag{6}$$

and the exponential-form PTT model

$$F(\boldsymbol{\tau})=\exp\left(\frac{\varepsilon\lambda}{\eta_p}\mathrm{Tr}\,(\boldsymbol{\tau})\right). \tag{7}$$

In (6) and (7), ε is a dimensionless parameter and $\mathrm{Tr}\,(\boldsymbol{\tau})$ is the trace of $\boldsymbol{\tau}$, i.e. the sum of its normal components. Note that for $\varepsilon=0$ both forms of the PTT model reduce to the Oldroyd-B model.

An alternative means to express the solvent viscosity and the polymeric viscosity is in terms of the total viscosity $\eta_{\mathrm{tot}}=\eta_s+\eta_p$ and the viscosity ratio

$$\beta=\frac{\eta_s}{\eta_s+\eta_p}. \tag{8}$$

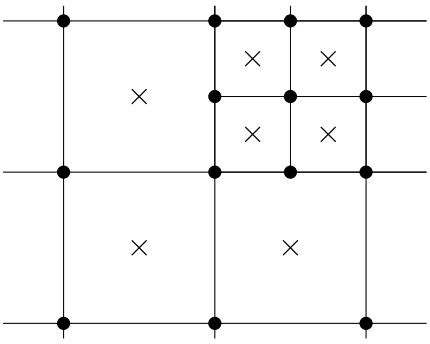

Fig. 1. Two-dimensional grid with one refinement level, showing cell centers (×) and grid nodes (•).

3. Numerical method

The numerical method to simulate viscoelastic flow is presented in condensed form in this section. A more detailed description of the backwards-tracking Lagrangian–Eulerian method is given in Ingelsten et al. [22].

The momentum Eq. (1) and the continuity Eq. (2) are discretized on a collocated Eulerian grid with the finite volume method and the pressure–velocity coupling is solved with the SIMPLEC method [34]. The solver combines a Cartesian octree or quadtree background grid, respectively for two or three dimensions, with implicit immersed boundary conditions for internal objects in the computational domain [35,36]. These objects can be arbitrarily located in the domain and do not need to align with the grid boundaries. The immersed boundary conditions are enforced through implicit mirroring of the velocity field inside the boundary surface. With the current approach, the handling of moving objects is straightforward.

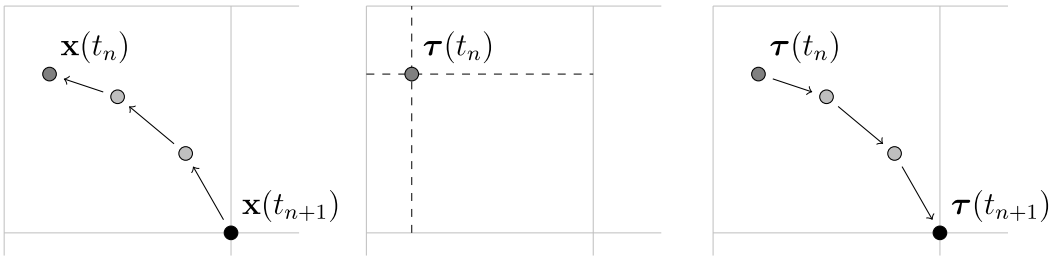

(a) Backwards-tracking. (b) Interpolation. (c) Forwards-solving.

Fig. 2. Schematic description of the steps involved in the backwards-tracking algorithm.

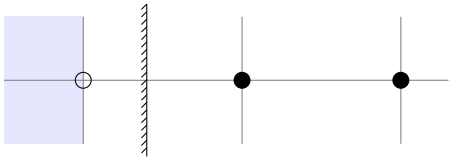

Fig. 3. Wall treatment with extrapolation node (∘), fluid nodes (•) wall and mirroring cells (filled).

All grid generation is automatic and the background grid is adaptively refined close to the solid walls and at the fluid–fluid interface. The grid is refined by recursively splitting cells in half in each dimension. In Fig. 1 an example of a two-dimensional grid with one refinement level is shown.

The viscoelastic constitutive Eq. (3) is solved in Lagrangian fluid elements, represented by nodes which are convected by the flow. The viscoelastic stress in a fluid element is described by the ordinary differential equation (ODE) system

$$\frac{D\boldsymbol{\tau}}{Dt} = \frac{2\eta_p}{\lambda}\mathbf{S} - \frac{1}{\lambda}F(\boldsymbol{\tau})\boldsymbol{\tau} + (\nabla\mathbf{u})^T\cdot\boldsymbol{\tau} + \boldsymbol{\tau}\cdot\nabla\mathbf{u}, \tag{9}$$

which follows from (3) and (4). Furthermore, since the local velocity gradient $\nabla\mathbf{u}$ appears on the right hand side of (9), the trajectory of the fluid element is required and is described by

$$\frac{D\mathbf{x}}{Dt} = \mathbf{u}, \tag{10}$$

where $\mathbf{x}$ is the position of the fluid element.

A backwards-tracking procedure, partly inspired by the BLPM by Wapperom et al. [10], is used to solve (9) and (10). The essence of the method is to explicitly choose the locations of the Lagrangian nodes at the end of a simulation step a priori to coincide with the Eulerian grid nodes. Thus, the connectivity of the Eulerian grid can be utilized for a structured and robust procedure to calculate the viscoelastic stress contribution to the fluid momentum.

Consider the calculation of the viscoelastic stress for the nth simulation time step, corresponding to $t \in I_n = [t_n, t_{n+1}]$. For a Lagrangian node, the trajectory backwards in time is given by

$$\mathbf{x}(t) = \mathbf{x}(t_{n+1}) - \int_t^{t_{n+1}} \mathbf{u}(t', \mathbf{x}(t'))dt', \quad t \in I_n, \tag{11}$$

where $\mathbf{x}(t_{n+1})$ is the position of the corresponding grid node. To calculate the new stress, the trajectory $\mathbf{x}(t)$, $t \in I_n$, is first calculated numerically by solving (10) backwards in time. Next, the viscoelastic stress $\boldsymbol{\tau}_n = \boldsymbol{\tau}(t_n, \mathbf{x}(t_n))$ is calculated from the previous stress field using bilinear or trilinear interpolation, respectively for two or three dimensions. The ODE system (9) is then solved forwards in time along the calculated trajectory to obtain the new stress $\boldsymbol{\tau}_{n+1} = \boldsymbol{\tau}(t_{n+1}, \mathbf{x}(t_{n+1}))$.

The velocities $\mathbf{u}$ are stored at the cell centers of the Eulerian grid and are interpolated with bilinear or trilinear interpolation, respectively for two or three dimensions, when required along the trajectories of the Lagrangian nodes. Similarly, the local velocity gradient $\nabla\mathbf{u}$ is calculated from the interpolation formula using the same basis. Further details are given in Ingelsten et al. [22].

A schematic description of the algorithm is shown in Fig. 2. In summary, the performed steps are:

(a) Calculate the Lagrangian node trajectory by solving (10) backwards in time, starting at the Eulerian grid node at $\mathbf{x}(t_{n+1})$.
(b) Interpolate the stress $\boldsymbol{\tau}(t_n, \mathbf{x}(t_n))$ to the Lagrangian node from the known stress field at time t_n.
(c) Solve (9) forwards in time along the trajectory $\mathbf{x}(t)$, $t \in I_n$.

Following previous work [22], the ODE systems (9) and (10) are solved with the fourth order Runge–Kutta RK4 method [37] with $N_{\text{sub}} = 3$ equidistant substeps per fluid time step. While the optimal choice of N_{sub} is not investigated in detail, it has been validated that a larger number does not affect the results for the flows considered in the current work.

Viscoelastic stresses in the vicinity of immersed boundary walls are calculated through extrapolation. Cells for which the center is located within half a cell length inside the immersed boundary are defined as mirror cells. In the Lagrangian stress algorithm, nodes which connect both mirroring cells and standard fluid cells are denoted extrapolation nodes. At such extrapolation nodes the constitutive equation is not solved. Instead, the viscoelastic stress is linearly extrapolated from the nodes inside the fluid. A geometric illustration is shown in Fig. 3.

The presence of two immiscible fluids, i.e. the viscoelastic fluid and a Newtonian fluid, is modeled with the volume of fluid (VOF) method, by solving the convection equation [38]

$$\frac{\partial\alpha}{\partial t} + \mathbf{u}\cdot\nabla\alpha = 0, \tag{12}$$

where $\alpha \in [0, 1]$ is the local volume fraction of viscoelastic fluid. Considering an Eulerian cell, for $\alpha = 1$ it is completely filled with the viscoelastic fluid and for $\alpha = 0$ it is filled with the Newtonian fluid. If $\alpha \in (0, 1)$ the cell intersects the interface between the two fluids, demonstrating the inherent diffuse-interface properties of the VOF method.

The finite volume method is used to discretize (12) on the Eulerian grid and the convection term is discretized with the compact CICSAM scheme [39]. The scheme is specifically designed to minimize the numerical diffusion of α and avoid smearing the fluid interface. Although two fluids are involved, a single set of Eqs. (1), (2) and (3) is solved. Local variations of fluid properties are accounted for through averaging on the form

$$\phi = \alpha\phi_v + (1-\alpha)\phi_N, \tag{13}$$

where ϕ_v and ϕ_N represent the properties of the viscoelastic and the Newtonian phase, respectively. This averaging is applied for the local properties η_p, λ and $\boldsymbol{\tau}$. When α is required at a Lagrangian node, the same interpolation scheme as for the velocities is used. To further improve numerical stability at the fluid–fluid interface, which may arise due to large velocity gradients in the low-viscous Newtonian phase, the

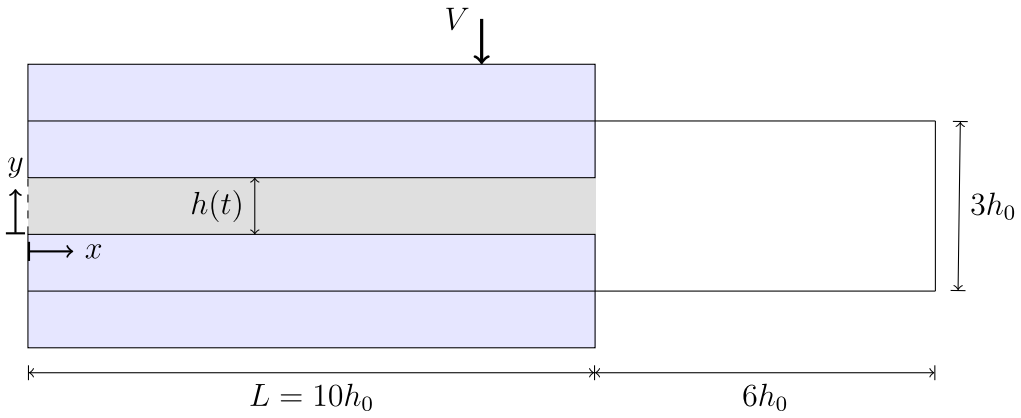

Fig. 4. Schematic of the squeezing flow between two plates. The gray area between the plates is initially filled with the viscoelastic fluid.

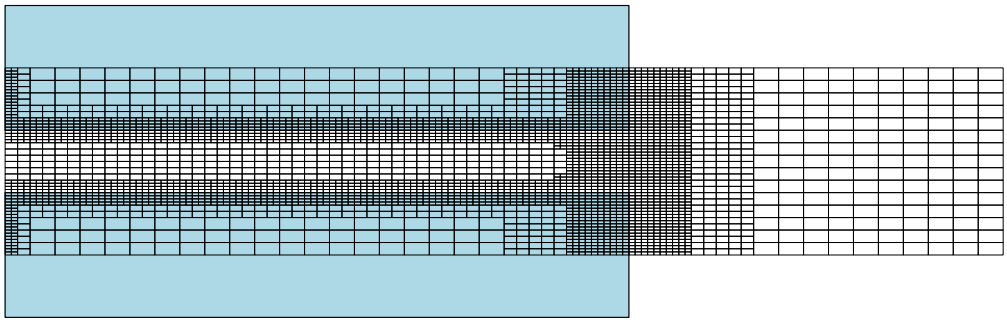

Fig. 5. The grid M1defined in Table 2 at $t = 0$.

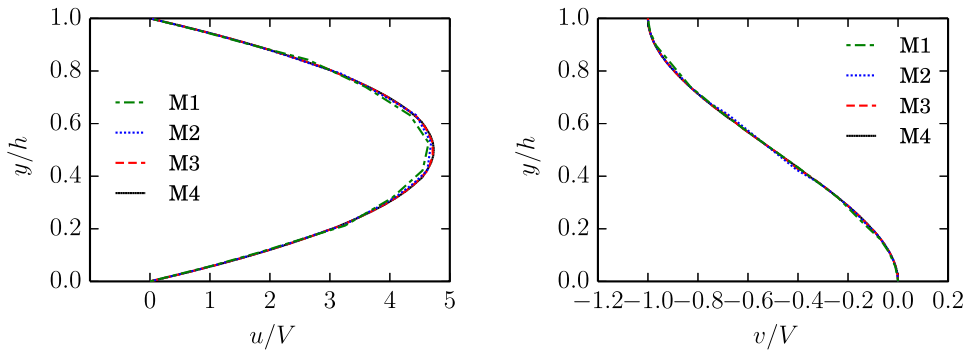

(a) u. (b) v.

Fig. 6. Velocity components (a) u and (6(b)) v between the plates at $x/h_0 = 3$ and $t^* = 0.05$ calculated for Wi = 1 with the grids defined in Table 2.

local values of ρ and η_s are calculated with a modified version of (13), reading

$$\tilde{\phi} = \tilde{\alpha}\phi_v + (1 - \tilde{\alpha})\phi_N, \tag{14}$$

where $\tilde{\alpha}$ is a modified volume fraction, which is intentionally smoothed in the Newtonian phase. For each computational cell, $\tilde{\alpha}$ is calculated as

$$\tilde{\alpha}_{i,k} = \begin{cases} \sum_f c_f \tilde{\alpha}_{f,k-1} & \text{if } \alpha_i < 0.01 \\ \alpha_i & \text{if } \alpha >= 0.01 \end{cases} \tag{15}$$

where $\tilde{\alpha}_{i,k}$ is the smoothed volume fraction in the ith cell at the kth smoothing step, such that $\tilde{\alpha}_{i,0} = \alpha_i$. The coefficient c_f is the inverse cell length in the normal direction of face f, normalized by the sum of the inverse cell lengths over the faces. Two smoothing steps are used, such that $\tilde{\alpha} = \tilde{\alpha}_2$ in (14). The procedure is an efficient and computationally cheap method to reduce the occurrence of large velocity gradients due to the low-viscous Newtonian phase, as well as the sensitivity to the large viscoelastic term in the momentum equation, near the fluid interface. It is remarked that the sole purpose of $\tilde{\alpha}$ is for the calculation of ρ and η_s. The volume fraction α solved for remains unmodified.

Following previous work, two threshold volume fractions are defined, denoted $\alpha_{\text{lim},1}$ and $\alpha_{\text{lim},2}$, respectively. Firstly, the viscoelastic constitutive equation is only solved for Eulerian grid nodes at which $\alpha > \alpha_{\text{lim},1}$. Secondly, cells for which $\alpha \leq \alpha_{\text{lim},2}$ are excluded from the calculation of the local velocity gradient along the Lagrangian node trajectories. The values $\alpha_{\text{lim},1} = 0.1$ and $\alpha_{\text{lim},2} = 0.01$ are used, and a more detailed description is given in Ingelsten et al. [22].

To couple the viscoelastic stress to the fluid momentum, the stress divergence is integrated over the fluid control volumes and added to the discretized form of the momentum Eq. (1). At this stage the product

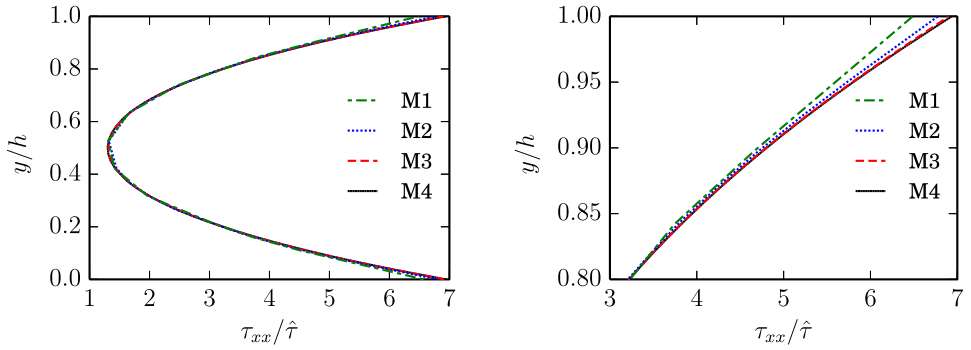

(a) Full. (b) Zoomed.

Fig. 7. Viscoelastic normal stress τ_{xx} between the plates at $x/h_0 = 3$ and $t^* = 0.05$ calculated for Wi = 1 with the grids defined in Table 2.

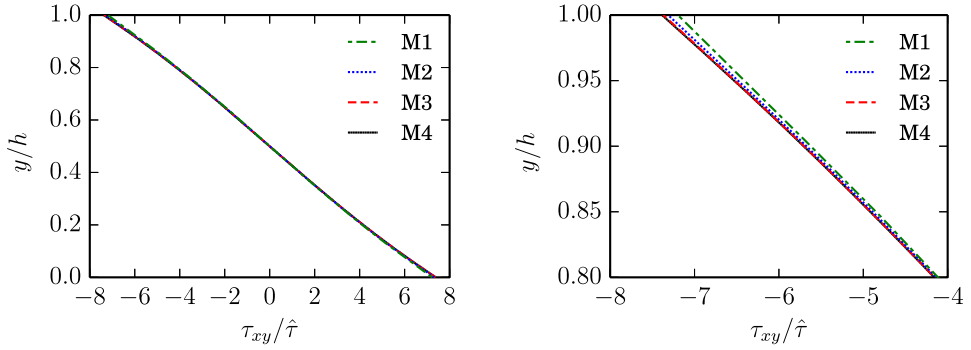

(a) Full. (b) Zoomed.

Fig. 8. Viscoelastic shear stress τ_{xy} between the plates at $x/h_0 = 3$ and $t^* = 0.05$ calculated for Wi = 1 with the grids defined in Table 2.

rule is applied, such that

$$\nabla \cdot (\alpha \boldsymbol{\tau}) = \alpha \nabla \cdot \boldsymbol{\tau} + \boldsymbol{\tau} \cdot \nabla \alpha. \tag{16}$$

This formulation may be interpreted as a separation of the pure interfacial contribution of the stress divergence term and the remainder part [40]. The first term of (16) is integrated with Gauss' divergence theorem as

$$\int_{\text{c.v.}} \nabla \cdot \boldsymbol{\tau} dV = \int_{\text{c.s.}} \hat{\mathbf{n}} \cdot \boldsymbol{\tau} dS = \sum_f \int_{\text{f.s.}} \hat{\mathbf{n}}_f \cdot \boldsymbol{\tau} dA, \tag{17}$$

where c.v. denotes the control volume, c.s. the surface of the control volume and $\hat{\mathbf{n}}$ the outwards surface normal. In the second step of (17) the surface integral is divided into a sum of the integrals over the respective cell faces f, with f.s. denoting the face surface and for which the normal $\hat{\mathbf{n}}_f$ is constant.

The face integrals are approximated with the trapezoidal rule using the stresses at the Eulerian grid nodes. For cell faces adjacent to smaller cells, e.g. as shown in Fig. 1, the sub-faces are integrated separately such that the stress at each grid node is included. The volume integral of the second term in (16) is approximated with the cell average stress and volume fraction gradient as

$$\int_{\text{c.v.}} (\boldsymbol{\tau} \cdot \nabla \alpha) dV \approx (\overline{\boldsymbol{\tau}} \cdot \overline{\nabla \alpha}) \Delta V, \tag{18}$$

where ΔV is the cell volume and $\overline{(\bullet)}$ denotes volume average. The volume average $\overline{\boldsymbol{\tau}}$ is calculated from the stresses at the nodes and $\overline{\nabla \alpha}$ is calculated with central differences. The threshold volume fraction $\alpha_{\text{lim},2}$ is again applied, such that the viscoelastic contribution is assumed to vanish in cells for which $\alpha < \alpha_{\text{lim},2}$ as they lie outside the viscoelastic phase.

It is remarked that the division of the stress divergence integral in (16) and the following approximations in (17) and (18) are used as the formulation has been found to enhance the numerical stability in combination with the threshold volume fractions $\alpha_{\text{lim},1}$ and $\alpha_{\text{lim},2}$.

To summarize the numerical method, the algorithm to simulate one fluid time step can be described as

1. Add the viscoelastic stress contribution to the discretized momentum equation.
2. Solve the momentum Eq. (1) and continuity Eq. (2) using SIMPLEC iterations.
3. Solve the transport of the fluid volume fraction α from (12)
4. Solve the viscoelastic constitutive Eq. (3) using the backwards-tracking procedure:
   (a) Calculate Lagrangian node trajectory through backwards-tracking.
   (b) Interpolate initial viscoelastic stress from previous time step.
   (c) Solve constitutive equation forwards in time along Lagrangian node trajectory.

4. Results

Simulation results from the described numerical method are presented in this section. The main focus of the current study is a viscoelastic squeeze flow. A brief study of the opposite case, in which the plate moves in the opposite direction, is also presented. Both cases are highly relevant for adhesive joining applications.

A schematic of the planar flow of a viscoelastic fluid squeezed between two parallel plates is given in Fig. 4. The lower plate is

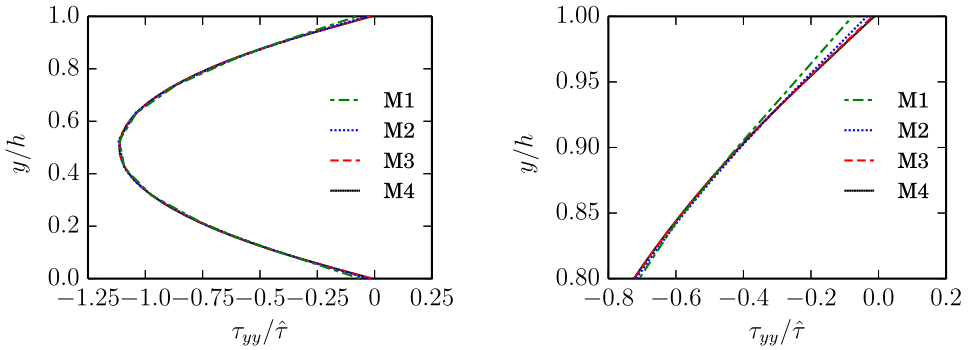

(a) Full. (b) Zoomed.

Fig. 9. Viscoelastic normal stress τ_{yy} between the plates at $x/h_0 = 3$ and $t^* = 0.05$ calculated for Wi = 1 with the grids defined in Table 2.

stationary and the upper plate moves with constant downward velocity V. The initial gap at $t = 0$ is denoted h_0 and, hence, the gap h varies with time as

$$h(t) = h_0 - Vt. \tag{19}$$

The plates have a length of $L = 10h_0$ in the x-direction and a thickness of $2h_0$ in the y-direction. The computational domain has a total length of $16h_0$ in the x-direction and $3h_0$ in the y-direction. An outlet boundary condition with $p = 0$ is imposed at the right domain boundary while the upper and lower domain boundaries are treated as walls with the no-slip condition. A symmetry condition is imposed at the left domain boundary. Hence, the case effectively describes flow between plates of length $2L$. At the stationary lower plate and at the moving upper plate the no-slip condition is imposed with the mirroring immersed boundary method.

A two-fluid flow is considered. At the start of the simulation the fluids are at rest and the gap between the plates is filled with the viscoelastic fluid. The area to the right of the plates is filled with a Newtonian gas, namely air with viscosity $\mu_{\text{air}} = 1.8205 \cdot 10^{-5}$ Pa s and density $\rho_{\text{air}} = 1.204$ kg/m^3. The effect of surface tension is neglected, as the primary focus is the viscoelastic effects. However, it is remarked that the current numerical framework has been employed to simulate flows with surface tension in previous studies, including with dynamic contact angle models [41].

Following previous work [11,13], the Weissenberg number is defined as

$$\text{Wi} = \frac{\lambda V}{h_0}, \tag{20}$$

and the Reynolds based on the solvent viscosity number as

$$\text{Re} = \frac{\rho V h_0}{\eta_s}. \tag{21}$$

The majority of the study is performed with the Oldroyd-B model. Simulations are also performed with the linear-form PTT model (6) and the exponential-form PTT model (7). The parameters for the viscoelastic fluid and for the flow, as well as the dimensionless groups, are summarized in Table 1. The physical parameters are representative for the intended applications, e.g. adhesive joining. It is noted that the density and viscosity ratios between the two phases are $\rho/\rho_{\text{air}} \approx 831$ and $\eta_{\text{tot}}/\mu_{\text{air}} \approx 5.5 \cdot 10^8$, respectively. Furthermore, it is remarked that the range of Weissenberg numbers covers four orders of magnitude.

The results in this section are presented as normalized quantities denoted by $(\bullet)^*$. Time is normalized by

$$\hat{t} = \frac{h_0}{V}, \tag{22}$$

i.e. the time it takes for the upper plate to fully close the gap with a constant velocity V. Stress and pressure are normalized by

$$\hat{\tau} = \frac{\eta_s V}{h_0}. \tag{23}$$

Table 1
Parameters and dimensionless numbers used for the viscoelastic squeeze flow.

Quantity	Value
L	0.1 m
h_0	0.01 m
V	0.1 m/s
η_{tot}	10^4 Pa s
β	1/9
λ	[0.001, 10] s
ε	[0, 0.5]
Wi	[0.01, 100]
Re	0.0009

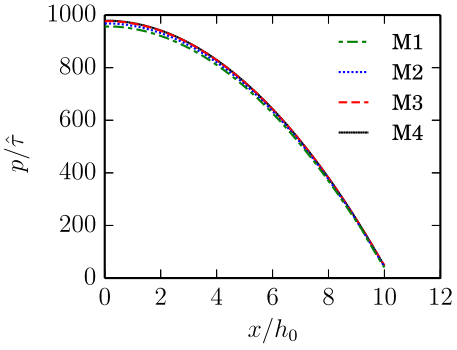

Fig. 10. Pressure along the gap at $y/h = 1/2$ and $t^* = 0.05$ calculated for Wi = 1 with the grids defined in Table 2.

A goal of the current study is to gain insight on the requirements on grid resolution to predict important flow quantities to a certain level of accuracy. To assess this, a grid dependence study is carried out using the Oldroyd-B model.

All grids used follow the same structure and are defined in terms of the base cell size $(\Delta x_{\max}, \Delta y_{\max})$, which is the size of the largest cells. Cells are refined for n_{ref} levels near the walls of the upper and lower plates as well as around the fluid interface for $0.05 < \alpha < 0.95$. The refinements are generated automatically and are adaptively updated throughout the simulation, as the upper plate and the fluid interface moves. The grids used are summarized in Table 2. For all grids $n_{\text{ref}} = 2$ and $\Delta x_{\max} = 2\Delta y_{\max}$. In Fig. 5 grid M1 is shown at $t = 0$. In the grid study, the flow is simulated for $0 \le t^* \le 0.05$ for $\text{Wi} = 0.01, 1, 100$ with the grids defined in Table 2, resulting in a total of 12 simulations. For all simulations, the time step Δt was chosen such that $V\Delta t/y_{\min} = 4 \cdot 10^{-4}$. To validate the step length, simulations with grid M2 and M3 has been repeated with half the step length. The results with the

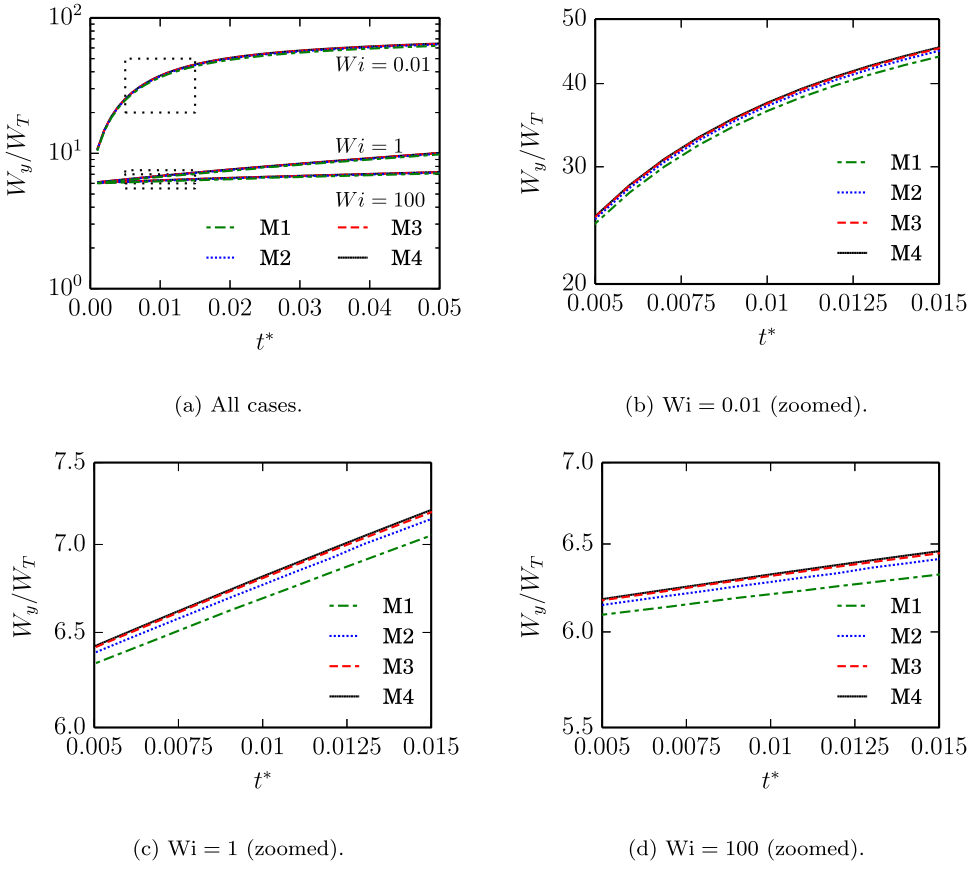

(a) All cases. (b) Wi = 0.01 (zoomed).

(c) Wi = 1 (zoomed). (d) Wi = 100 (zoomed).

Fig. 11. Simulated forces calculated with the grids defined in Table 2.

Table 2
Grids used in the grid study.

Grid	$h_0/\Delta y_{\max}$	$h_0/\Delta y_{\min}$	n_{ref}
M1	5	20	2
M2	10	40	2
M3	20	80	2
M4	40	160	2

different step lengths overlap, confirming that the chosen step length is sufficiently small.

In Fig. 6 the velocity components u and v, respectively in the x- and y-directions, are shown across the gap at $x/h_0 = 3$ for Wi = 1 at $t^* = 0.05$. The corresponding viscoelastic stresses τ_{xx}, τ_{xy} and τ_{yy} are shown in Fig. 7, Fig. 8 and Fig. 9, respectively. For the stresses, zoomed in views near the moving upper plate are also given. As indicated by the small Reynolds number in Table 1, the inertial effects are small and the flow features a symmetry about the center of the gap at $y = h/2$. For both the velocities and the stresses, the profiles obtained with the different grids are close and tend towards the solution from the finest grid M4 with increasing resolution. Observing at the zoomed scales, slight differences between the results on the different grids are revealed for the viscoelastic stresses near the wall. The solution from the coarsest grid M1 particularly stands out, while those from the two finer grids M3 and M4 practically overlap. Moreover, the results from grid M2 is reasonably close to those from the two finest grids. The corresponding results for Wi = 0.01 and Wi = 100 are very similar to those for Wi = 1 and can be found in the supplementary material.

In Fig. 10 the pressure profiles along the gap centerline $y/h = 1/2$ obtained for Wi = 1 with the grids defined in Table 2 are shown. The same trends observed for the velocities and stresses are found for the pressure. At the scale of comparison, the pressure computed with the different grids are close, particularly for those computed with the three finest grids.

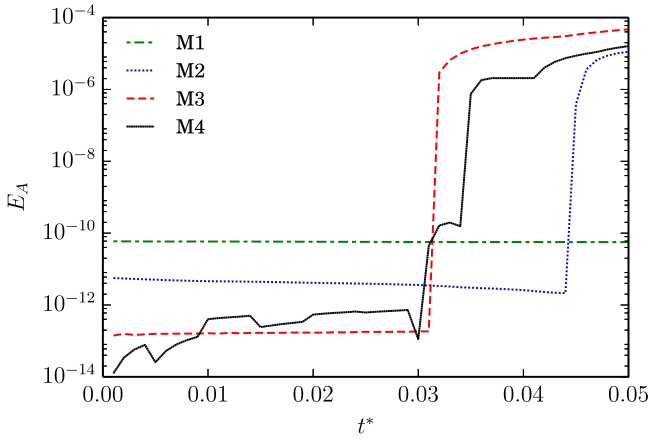

Fig. 12. Calculated relative area error for the grids defined in Table 2 simulated with Wi = 1.

A quantity of particular interest, not the least in the context of e.g. adhesive joining operations, is the load exerted by the viscoelastic fluid on the solid parts. The load exerted by a fluid on an object is given by the integral of the fluid stress over the object surface, as

$$\mathbf{W} = \int_S (-p\mathbf{I} + \boldsymbol{\tau} + 2\eta_s \mathbf{S}) \cdot \hat{\mathbf{n}} dS, \tag{24}$$

where $\hat{\mathbf{n}}$ is the local surface normal. The main contribution to the load is that in the y-direction on the horizontal surface in the gap, for which

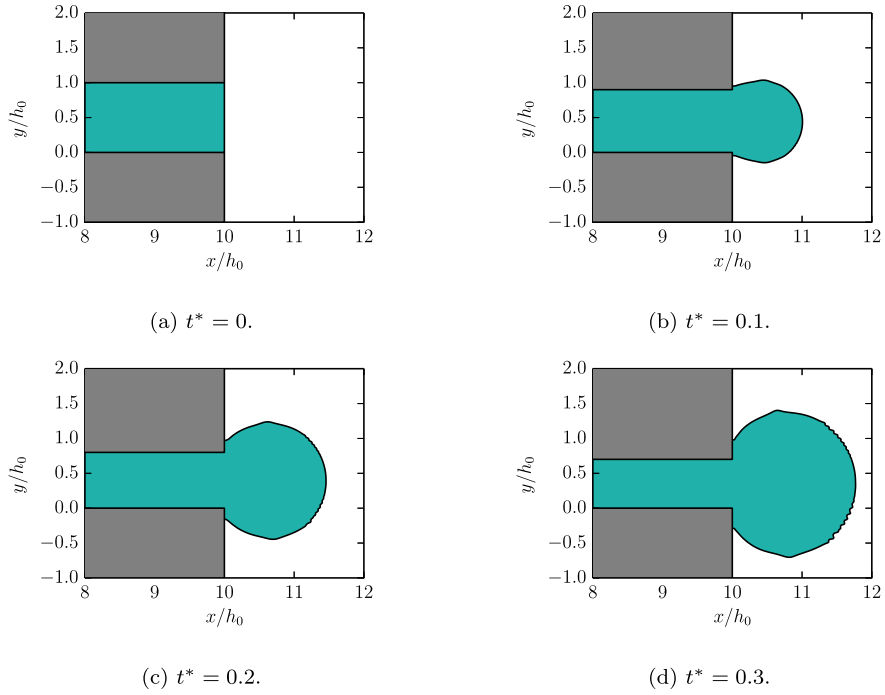

(a) $t^* = 0$. (b) $t^* = 0.1$.

(c) $t^* = 0.2$. (d) $t^* = 0.3$.

Fig. 13. Snapshots of simulation for Wi = 1 with grid M3 showing the interface between the viscoelastic fluid (green) and the air (white) visualized by $\alpha = 0.5$.

(24) simplifies to

$$W_y = \int_0^L (p - \tau_{yy} - \eta_p \frac{\partial v}{\partial y}) dL. \tag{25}$$

Since the viscoelastic and the viscous terms respectively tend to zero at the wall, the load is expected to be dominated by the fluid pressure p. Note, however, that the loads presented in this section are all calculated with (24).

In Fig. 11 the y-directional loads on the upper plate simulated with the grids defined Table 2 for Wi $= 0.01, 1, 100$ are shown for $0 \leq t^* \leq 0.05$. At the scale of comparison, the loads predicted with all grids are very close and a zoomed in comparison is therefore given for each Wi.

Grid convergence is observed and the loads predicted with the two finest grids M3 and M4 are very close for all three cases. Again, the results obtained with grid M2 are reasonably close to those from the finer grids, particularly at the global scale of comparison in Fig. 11. This observation is important for engineering applications and industrial scale cases, as computational cost is often a limiting factor. The ability to obtain acceptable force predictions also for coarser grids, and thus at a lower computational cost, is therefore a big advantage.

Mass conservation is briefly assessed in terms of the integrated area

$$A_v = \int_\Omega \alpha dA = \sum_{i=1}^{N_{\text{cells}}} \alpha_i A_i, \tag{26}$$

where Ω denotes the computational domain, N_{cells} the number of fluid cells, α_i the volume fraction in the ith cell and A_i the area of the cell which is does not include any immersed boundaries. The relative error with respect to the initial area is calculated as $E_A = |A_v/A_0 - 1|$, where A_0 is the area at $t = 0$. In Fig. 12 the area errors obtained for Wi $= 1$ with the grids in Table 2 are shown for $t^* \in [0, 0.05]$. Initially, the errors are extremely small, while they increase as the viscoelastic fluid starts to emerge from the gap. The slight difference in behavior between the grids is likely due to the automatic grid adaptation, since the grid updates depend on the cell sizes. For grid M2 , for which simulations have also been performed for $t^* \in [0, 0.5]$, the maximum observed error is 0.062%. Thus, the observed mass errors are small and may be assumed to not affect the simulation outcome.

So far, the simulations have been carried out for time $0 \leq t^* \leq 0.05$. Further on, results from longer simulations are also reported. The focus is mainly on the load exerted on the upper plate and, given the results from the grid dependence study, the simulations are mainly carried out with grid M2 . In Fig. 13 snapshots of a simulation performed with grid M3 for Wi $= 1$ are shown, where the two fluid phases are visualized. As the gap decreases due to the upper plate movement, a certain amount of viscoelastic fluid is squeezed out and exhibits swelling. This observation highlights the relevance of including the two-fluid model in the framework, as the presence of such effects may be of importance for practical applications. The details of the swelling effect are not discussed in detail in the current work. However, it is noted that the viscoelastic die swell effect has been previously simulated with the current numerical method [22].

To validate the results obtained for the viscoelastic squeeze flow, they are compared to the theoretical predictions presented by Phan-Thien and coworkers [11,13]. They studied squeeze-film flow between plates in planar and axisymmetric configurations for different viscoelastic constitutive models. In their work, it was assumed that the velocities u and v may be expressed as

$$v(t, y) = V f(t, y), \tag{27}$$

$$u(t, x, y) = -xV \frac{\partial f}{\partial y}, \tag{28}$$

where f is a function. The expression (27) stems from the assumption that material planes which are initially parallel to the plates remain parallel [19], such that v is a function only of t and y. Then (28) follows from the continuity Eq. (2).

Expressions for the load on the upper plate for the limiting cases Wi $\to 0$ and Wi $\to \infty$ were obtained using perturbation theory. For the complete derivation, the reader is referred to the original work [12,13]. The resulting expressions used in the current work for comparison are stated here for completeness. Assuming a plate moving with constant velocity V, the load on $0 \leq x \leq L$ for Wi $\to 0$ is given by

$$\frac{W_y}{W_T} = \frac{6(1+b)}{H^3} + \frac{51}{35}\frac{\text{Re}}{H^2} + O\left(\text{Re}^2, \text{ReWi}, \text{Wi}^2\right), \tag{29}$$

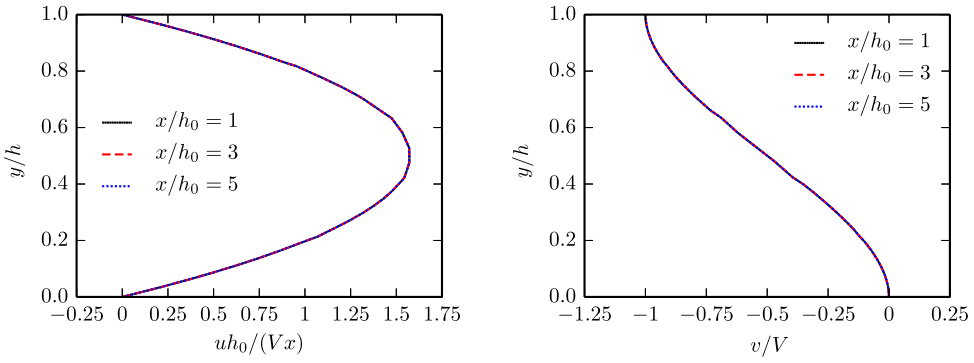

(a) u. (b) v.

Fig. 14. Velocity profiles across the gap for Wi = 1 at different horizontal positions at $t^* = 0.05$, obtained with grid M3.

and for Wi → ∞

$$\frac{W_y}{W_T} = \frac{6}{H^3} + \frac{51}{35}\frac{\mathrm{Re}}{H^2} + O\left(\mathrm{Re}^2, \frac{1}{\mathrm{Wi}}\right), \tag{30}$$

where $W_T = 2\eta_s V L^3/(3h_0^3)$, $H = h/h_0$ and $b = \eta_p/\eta_s$. In (29) and (30) the plate length L is assumed to be large, such that end effects may be neglected.

It is noted that for this particular case, the only difference between (29) and (30) is the influence of the viscosity ratio, through the ratio $b = \eta_p/\eta_s$. Furthermore, the expressions (29) and (30) actually correspond to the behavior of Newtonian fluids, with viscosity $\eta_p + \eta_s$ and η_s, respectively.

As a first validation, the velocity profiles between the plates are shown at different locations in order to test the agreement with the assumptions (27) and (28). According to (27), the vertical velocity profile v is a function only of t and y. Similarly, according to (28) the profiles of u divided by the horizontal coordinate x is also a function of only t and y. Consequently, these profiles of at different horizontal locations are expected to overlap. In Fig. 14 the streamwise velocity u divided by the horizontal coordinate x/h_0 and the vertical velocity y are shown across the gap between the plates for Wi = 1 at $x/h_0 = 1, 3, 5$ and $t^* = 0.05$. Clearly, the profiles overlap, indicating that the simulations agree with (27) and (28). The corresponding results for Wi = 0.01 and Wi = 100 are virtually identical and can be found in the supplementary material.

In Fig. 15 the calculated loads on the upper plate for $0 \le t^* \le 0.5$ for Oldroyd-B fluids with Wi = $0.01, 0.1, 0.3, 1, 10, 100$ are shown. The simulations have been performed with grid M2 . The asymptotic loads for Wi → 0 and Wi → ∞ are included for comparison. For Wi = 0.01, the simulated load approaches the asymptotic curve for Wi → 0 after a short time. It is also noted that the initial period of rapid change is on the order of the relaxation time. For Wi = 0.1, a similar initial transient during the first relaxation time is observed, before reaching a behavior which is similar to the asymptotic curve, however of different magnitude. At the opposite end of Weissenberg number range, the simulated load for Wi = 100 follows the asymptotic curve for Wi → ∞ closely. Furthermore, the predicted load for Wi = 10 is relatively close to the load for Wi = 100. The results indicate that Wi ≤ 0.01 approximately fulfills the condition Wi → 0, provided that the initial transient is ignored. Similarly, Wi → ∞ is approximately fulfilled for Wi ≥ 100. As a remark, these results agree qualitatively with those reported by Debbaut et al. [14] and by Phan-Thien et al. [13], who reported the same trends for the corresponding axisymmetric flow.

The influence of different fluid properties is further tested through a set of simulations with the PTT model, both in the linear form (6) and in the exponential form (7). Due to the nonlinear nature of the PTT model, it involves shear-thinning and is arguably a more suitable model for many real-life viscoelastic fluids, compared to the Oldroyd-B model.

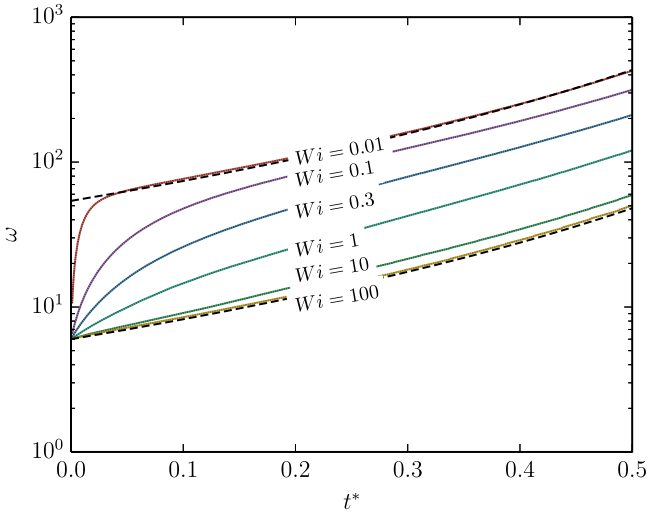

Fig. 15. Predicted loads on upper plate for Oldroyd-B fluids simulated using grid M2, as well as asymptotic loads (dashed lines) for Wi → 0 and Wi → ∞.

First, the Oldroyd-B model and the PTT model are compared for different Wi. In Fig. 16 the load on the upper plate simulated for $0 \le t^* \le 0.5$ with the linear and exponential form PTT models are compared for Wi = $0.01, 1, 100$ using $\varepsilon = 0$ and $\varepsilon = 0.05$. Note that for $\varepsilon = 0$ the PTT model is identical to the Oldroyd-B model.

As expected, both forms of the PTT model yield smaller loads than the corresponding Oldroyd-B model, due to the shear-thinning properties. The effect is the most pronounced for Wi = 1, while for Wi = 0.01 and Wi = 100, the loads are very close to those predicted by the Oldroyd-B model. Furthermore, the shear-thinning is practically negligible for $t^* < 0.1$ but increases with time. The effect is stronger for the exponential-form PTT model, since the nonlinear term $F(\boldsymbol{\tau})$ grows faster with the stress trace compared to linear-form PTT model. The onset of shear-thinning also appears earlier for the exponential form.

In Fig. 17 the loads on the upper plate simulated for $0 \le t^* \le 0.5$ for Wi = 1 using $\varepsilon = 0, 0.05, 0.1, 0.25, 0.5$. In consistency with the previous observations, the shear thinning increases with time and is generally stronger for the exponential form PTT model. The largest difference is observed between $\varepsilon = 0$ and $\varepsilon = 0.05$ and the onset of shear-thinning appears earlier for increasing ε. Again, the effect is stronger for the exponential form model.

While the current work is mainly focused on squeeze flow, the opposite case, here referred to as reverse squeeze flow, is relevant for adhesive joining applications as well. One example is the springback effect in during the hemming process. In hemming applications, two

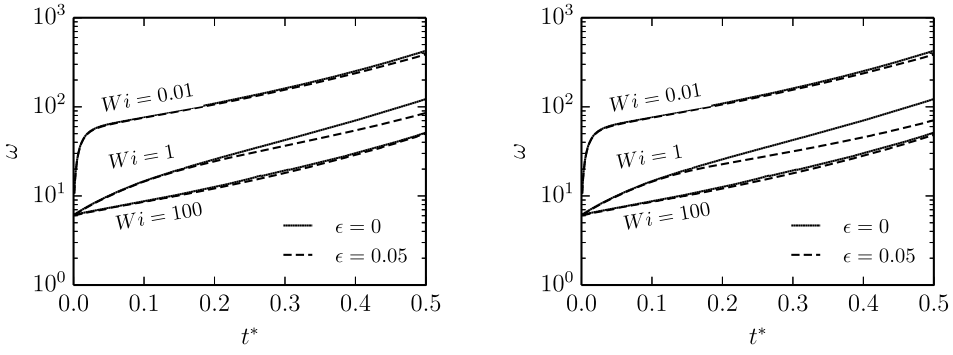

(a) PTT linear. (b) PTT exponential.

Fig. 16. Simulated loads with for Wi = 0.01, 1, 100 calculated using grid M2 defined in Table 2 for (a) the linear form PTT model and (b) the exponential form PTT model.

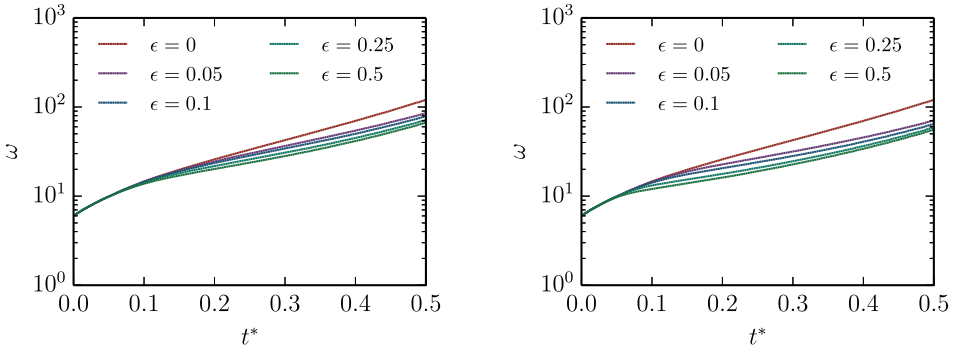

(a) PTT linear. (b) PTT exponential.

Fig. 17. Simulated loads with for Wi = 1 calculated using grid M2 defined in Table 2 with (a) the linear form PTT model and (b) the exponential form PTT model.

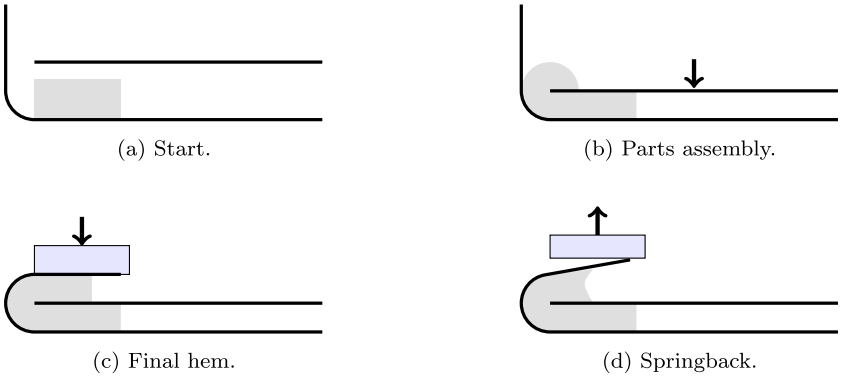

Fig. 18. Illustration of hemming process.

panels are first joined through assembly with an adhesive. This is followed by a forming step, in which the outer panel is folded around the inner panel. At this point, however, the outer panel may recover a part of the deformation. This effect, commonly referred to as springback, may impact the quality of the joint, e.g. by reducing the degree of filling of adhesive. An illustration of the effect is given in Fig. 18.

In the current work, a conceptual representation of the adhesive flow during springback is taken as the reverse squeeze flow for the configuration in Fig. 4, with the upper plate now instead moving upwards with velocity V. To reveal the dependence on viscoelastic fluid properties, the flow is simulated with the Oldroyd-B model and the exponential-form PTT model with Wi = $0.01, 0.1, 0.3, 1, 10, 100$ for $t^* \in [0, 0.2]$ using grid M2 . For the PTT model, $\varepsilon = 0.05$ is used. In Fig. 19 snapshots from the simulation with the Oldroyd-B model and Wi = 1 are shown. The increase of volume between the plates results in a drastic change of geometry for the viscoelastic fluid even for a relatively small movement. In the context of hemming, this demonstrates how springback may impact e.g. the degree of filling in the joint.

The magnitude of the loads on the upper plate for the reverse squeeze flow, which act in the negative y-direction, are shown in Fig. 20. A similar spread between the different Weissenberg numbers as for the squeeze flow previously studied is found, as well as initial transients which occur approximately during the first relaxation time of the flow. With exception for the initial transient behavior, the loads decrease over time. As shown by the loads for the PTT model, the decrease is enhanced by shear thinning and is the most pronounced for the moderate Weissenberg numbers. In the context of hemming, this indicates a decreasing resistance to the springback. The simulations

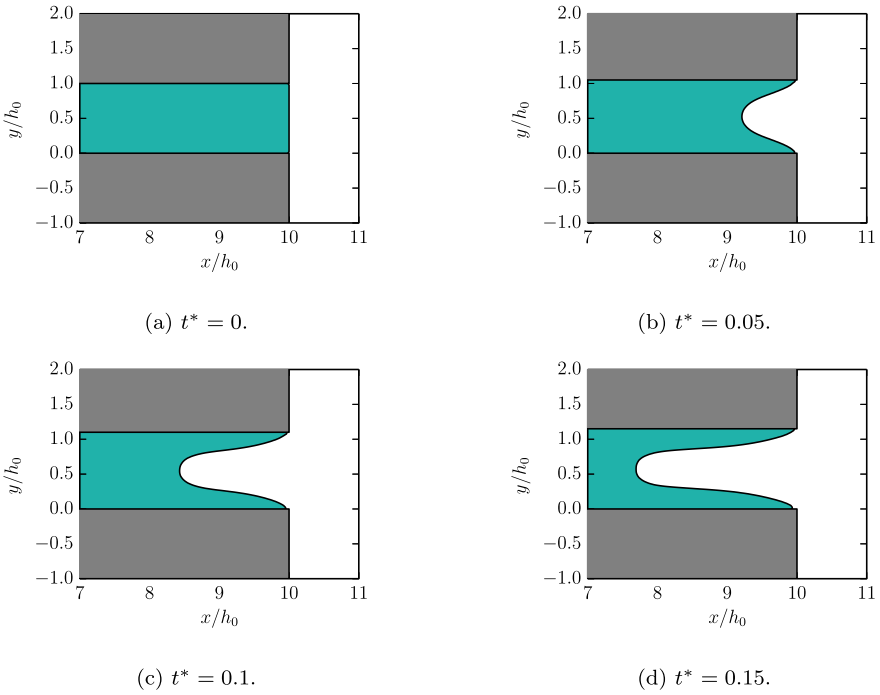

(a) $t^* = 0$. (b) $t^* = 0.05$.

(c) $t^* = 0.1$. (d) $t^* = 0.15$.

Fig. 19. Snapshots of reverse squeeze simulation for Wi = 1 with grid M2 showing the interface between the viscoelastic fluid (green) and the air (white) visualized by $\alpha = 0.5$.

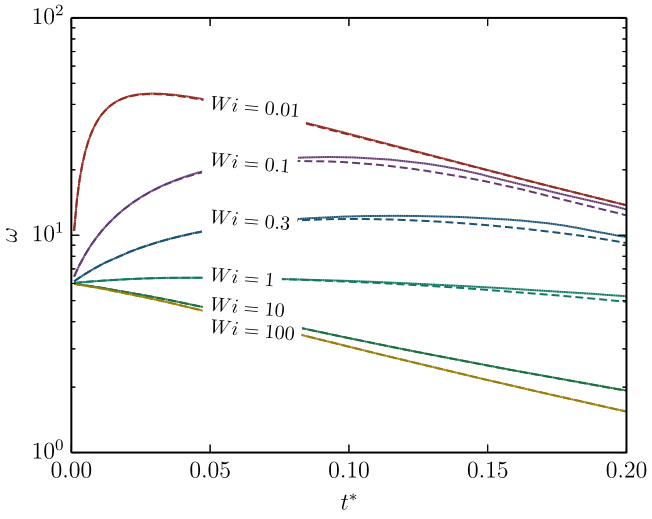

Fig. 20. Simulated loads for reverse squeeze flow for the Oldroyd-B model (solid lines) and for the exponential PTT model with $\epsilon = 0.05$ (dashed lines) calculated using grid M2 defined in Table 2.

thus highlight, albeit on a conceptual level, how the viscoelastic fluid properties may directly impact adhesive joint quality.

5. Conclusions

A backwards-tracking Lagrangian–Eulerian method has been employed to simulate planar viscoelastic squeeze flow, which involves free surfaces as well as moving solid boundaries. The flow is of high industrial relevance and has important implications e.g. for adhesive joining applications, such as parts assembly and hemming. The goal of the study was to validate the numerical method for such flows, as well as to assess the grid requirements for prediction of important flow quantities.

A grid dependence study was performed for a wide range of Weissenberg numbers, covering four orders of magnitude. It was found that fairly high resolution is required to resolve the viscoelastic stress in the gap due to steep gradients near the upper plate. However, in contrast to this, an important conclusion was that the load exerted on the upper plate can be predicted to reasonable accuracy with a relatively coarse grid. This has important implications for engineering applications, since the ability to qualitatively compare different fluid properties or flow configurations to a low computational cost can be crucial to enable the productive use of numerical simulations. Furthermore, in many applications, detailed knowledge about the stress field in the gap may be disregarded while the load exerted on the product production equipment may be important.

The main part of the study was performed for the Oldroyd-B model. The simulated results were validated by theoretical predictions from the literature and were found to be in excellent agreement with the available theory. Furthermore, they qualitatively resembled similar numerical results from the literature for the Oldroyd-B model across the wide range of Weissenberg numbers. The same flow was then simulated with the linear- and exponential-form PTT models. The simulations revealed a strong influence of shear-thinning for moderate Weissenberg numbers, which increased with time. Finally, a reverse squeeze flow was simulated as a simple representation of the springback effect in hemming applications, demonstrating geometrical aspects of the viscoelastic adhesive as well as the load on the upper plate. The simulations highlighted how different viscoelastic fluid properties may impact the quality of adhesive joints on a conceptual level. More importantly, the results indicated that similar results for industrial cases may be valuable in the production design process.

Although simple in concept, the studied flows involve complex combinations of shear and extensional flow of a viscoelastic fluid. A majority of numerical methods for fluid flow simulations involve a body conforming discretization. Hence, treatment of moving geometries may result in a distorted mesh due to deformation, or require advanced techniques such as moving meshes. In contrast, applying the current method for more complex cases is fairly straightforward, due to the combination of the immersed boundary method and the adaptive octree grid. The current study has therefore strongly indicated a great potential towards real, industrial applications. In future research, the numerical framework will be utilized for industrial adhesive joining

applications such as parts assembly and hemming, which include more complex geometries as well as viscoelastic fluids.

Declaration of competing interest

The authors declare that they have no known competing financial interests or personal relationships that could have appeared to influence the work reported in this paper.

Acknowledgments

This research has been partly carried out in a Centre for Additive Manufacturing — Metal (CAM2) in a joint project financed by Swedish Governmental Agency of Innovation Systems (Vinnova), Sweden, coordinated by Chalmers University of Technology. The work has also been supported in part by Vinnova through the FFI Sustainable Production Technology program and the project "Virtual Verification of the Hemming Process", and in part by the Chalmers Area of Advance Production, Sweden. The support is gratefully acknowledged.

References

[1] P. Oliveira, F. Pinho, G. Pinto, Numerical simulation of non-linear elastic flows with a general collocated finite-volume method, J. Non-Newton. Fluid Mech. 79 (1) (1998) 1–43, http://dx.doi.org/10.1016/S0377-0257(98)00082-2.

[2] M. Alves, F. Pinho, P. Oliveira, The flow of viscoelastic fluids past a cylinder: finite-volume high-resolution methods, J. Non-Newton. Fluid Mech. 97 (2) (2001) 207–232, http://dx.doi.org/10.1016/S0377-0257(00)00198-1.

[3] M.A. Alves, P.J. Oliveira, F.T. Pinho, Benchmark solutions for the flow of Oldroyd-B and PTT fluids in planar contractions, J. Non-Newton. Fluid Mech. 110 (1) (2003) 45–75, http://dx.doi.org/10.1016/S0377-0257(02)00191-X.

[4] H.P. Baaijens, G.W. Peters, F.P. Baaijens, H.E. Meijer, Viscoelastic flow past a confined cylinder of a polyisobutylene solution, J. Rheol. 39 (6) (1995) 1243–1277.

[5] M.A. Hulsen, R. Fattal, R. Kupferman, Flow of viscoelastic fluids past a cylinder at high Weissenberg number: Stabilized simulations using matrix logarithms, J. Non-Newton. Fluid Mech. 127 (1) (2005) 27–39, http://dx.doi.org/10.1016/j.jnnfm.2005.01.002.

[6] H. Rasmussen, O. Hassager, Simulation of transient viscoelastic flow with second order time integration, J. Non-Newton. Fluid Mech. 56 (1) (1995) 65–84, http://dx.doi.org/10.1016/0377-0257(94)01274-L.

[7] O. Harlen, J. Rallison, P. Szabo, A split Lagrangian-Eulerian method for simulating transient viscoelastic flows, J. Non-Newton. Fluid Mech. 60 (1) (1995) 81–104, http://dx.doi.org/10.1016/0377-0257(95)01381-5.

[8] P. Halin, G. Lielens, R. Keunings, V. Legat, The Lagrangian particle method for macroscopic and micro–macro viscoelastic flow computations dedicated to professor Marcel J. Crochet on the occasion of his 60th birthday.1, J. Non-Newton. Fluid Mech. 79 (2) (1998) 387–403, http://dx.doi.org/10.1016/S0377-0257(98)00123-2.

[9] X. Gallez, P. Halin, G. Lielens, R. Keunings, V. Legat, The adaptive Lagrangian particle method for macroscopic and micro–macro computations of time-dependent viscoelastic flows, Comput. Methods Appl. Mech. Engrg. 180 (3) (1999) 345–364, http://dx.doi.org/10.1016/S0045-7825(99)00173-5.

[10] P. Wapperom, R. Keunings, V. Legat, The backward-tracking Lagrangian particle method for transient viscoelastic flows, J. Non-Newton. Fluid Mech. 91 (2) (2000) 273–295, http://dx.doi.org/10.1016/S0377-0257(99)00095-6.

[11] N. Phan-Thien, R.I. Tanner, Viscoelastic squeeze-film flows – Maxwell fluids, J. Fluid Mech. 129 (1983) 265–281, http://dx.doi.org/10.1017/S0022112083000762.

[12] N. Phan-Thien, R.I. Tanner, Lubrication squeeze-film theory for the Oldroyd-B fluid, J. Non-Newton. Fluid Mech. (1984).

[13] N. Phan-Thien, J. Dudek, D. Boger, V. Tirtaatmadja, Squeeze film flow of ideal elastic liquids, J. Non-Newton. Fluid Mech. 18 (3) (1985) 227–254, http://dx.doi.org/10.1016/0377-0257(85)87001-4, URL https://www.sciencedirect.com/science/article/pii/0377025785870014.

[14] B. Debbaut, Non-isothermal and viscoelastic effects in the squeeze flow between infinite plates, J. Non-Newton. Fluid Mech. 98 (1) (2001) 15–31, http://dx.doi.org/10.1016/S0377-0257(01)00096-9, URL https://www.sciencedirect.com/science/article/pii/S0377025701000969.

[15] Ansys polyflow, URL https://www.ansys.com/products/fluids/ansys-polyflow.

[16] M. Shafahi, N. Ashrafi, Numerical investigation of a non-Newtonian fluid squeezed between two parallel disks, Korea-Australia Rheol. J. 32 (2) (2020) 89–97, http://dx.doi.org/10.1007/s13367-020-0002-9.

[17] H.M. Duwairi, B. Tashtoush, R.A. Damseh, On heat transfer effects of a viscous fluid squeezed and extruded between two parallel plates, Heat Mass Transf. 41 (2) (2004) 112–117, http://dx.doi.org/10.1007/s00231-004-0525-5.

[18] P. Kaushik, P.K. Mondal, S. Chakraborty, Flow dynamics of a viscoelastic fluid squeezed and extruded between two parallel plates, J. Non-Newton. Fluid Mech. 227 (2016) 56–64, http://dx.doi.org/10.1016/j.jnnfm.2015.11.007, URL https://www.sciencedirect.com/science/article/pii/S0377025715001998.

[19] J. Engmann, C. Servais, A.S. Burbidge, Squeeze flow theory and applications to rheometry: A review, J. Non-Newton. Fluid Mech. 132 (1) (2005) 1–27, http://dx.doi.org/10.1016/j.jnnfm.2005.08.007, URL https://www.sciencedirect.com/science/article/pii/S0377025705001977.

[20] S. Ingelsten, A. Mark, F. Edelvik, A Lagrangian-Eulerian framework for simulation of transient viscoelastic fluid flow, J. Non-Newton. Fluid Mech. 266 (2019) 20–32, http://dx.doi.org/10.1016/j.jnnfm.2019.02.005.

[21] S. Ingelsten, A. Mark, K. Jareteg, R. Kádár, F. Edelvik, Computationally efficient viscoelastic flow simulation using a Lagrangian-Eulerian method and GPU-acceleration, J. Non-Newton. Fluid Mech. (2020) 104264, http://dx.doi.org/10.1016/j.jnnfm.2020.104264.

[22] S. Ingelsten, A. Mark, R. Kádár, F. Edelvik, A backwards-tracking Lagrangian-Eulerian method for viscoelastic two-fluid flows, Appl. Sci. 11 (1) (2021) http://dx.doi.org/10.3390/app11010439, URL https://www.mdpi.com/2076-3417/11/1/439.

[23] IPS IBOFlow, http://ipsiboflow.com.

[24] F. Edelvik, A. Mark, N. Karlsson, T. Johnson, J. Carlson, Math-based algorithms and software for virtual product realization implemented in automotive paint shops, in: L. Ghezzi, D. Hömberg, C. Landry (Eds.), Math for the Digital Factory, Springer-Verlag, Berlin, 2017, pp. 231–251.

[25] A. Mark, R. Bohlin, D. Segerdahl, F. Edelvik, J.S. Carlson, Optimisation of robotised sealing stations in paint shops by process simulation and automatic path planning, Int. J. Manuf. Res. 9 (1) (2014) 4–26, http://dx.doi.org/10.1504/IJMR.2014.059597.

[26] M. Svensson, A. Mark, F. Edelvik, J. Kressin, R. Bohlin, D. Segerdahl, J.S. Carlson, P.-J. Wahlborg, M. Sundbäck, Process simulation and automatic path planning of adhesive joining, Procedia CIRP 44 (2016) 298–303, http://dx.doi.org/10.1016/j.procir.2016.02.113, 6th CIRP Conference on Assembly Technologies and Systems (CATS).

[27] J. Göhl, K. Markstedt, A. Mark, K. Håkansson, P. Gatenholm, F. Edelvik, Simulations of 3D bioprinting: predicting bioprintability of nanofibrillar inks, Biofabriaction 10 (2018) http://dx.doi.org/10.1088/1758-5090/aac872.

[28] E. Svenning, A. Mark, F. Edelvik, Simulation of a highly elastic structure interacting with a two-phase flow, J. Math. Ind. 4 (1) (2014) 7, http://dx.doi.org/10.1186/2190-5983-4-7.

[29] A. Mark, E. Svenning, F. Edelvik, An immersed boundary method for simulation of flow with heat transfer, Int. J. Heat Mass Transfer 56 (1–2) (2013) 424–435, http://dx.doi.org/10.1016/j.ijheatmasstransfer.2012.09.010.

[30] T. Andersson, D. Nowak, T. Johnson, A. Mark, F. Edelvik, K.-H. Küfer, Multiobjective optimization of a heat-sink design using the sandwiching algorithm and an immersed boundary conjugate heat transfer solver, J. Heat Transfer 140 (10) (2018) http://dx.doi.org/10.1115/1.4040086, 102002.

[31] D. Nowak, T. Johnson, A. Mark, C. Ireholm, F. Pezzotti, L. Erhardsson, D. Ståhlberg, F. Edelvik, K.-H. Küfer, Multicriteria optimization of an oven with a novel ϵ-constraint-based sandwiching method, J. Heat Transfer 143 (1) (2020) http://dx.doi.org/10.1115/1.4048737, 012101.

[32] R.G. Larson, Constitutive Equations for Polymer Melts and Solutions, in: Butterworths series in chemical engineering, Butterworth Publishers, 1988.

[33] N.P. Thien, R.I. Tanner, A new constitutive equation derived from network theory, J. Non-Newton. Fluid Mech. 2 (4) (1977) 353–365.

[34] J.P.V. Doormaal, G.D. Raithby, Enhancements of the simple method for predicting incompressible fluid flows, Numer. Heat Transfer 7 (2) (1984) 147–163, http://dx.doi.org/10.1080/01495728408961817.

[35] A. Mark, B.G.M. van Wachem, Derivation and validation of a novel implicit second-order accurate immersed boundary method, J. Comput. Phys. 227 (2008) 6660–6680.

[36] A. Mark, R. Rundqvist, F. Edelvik, Comparison between different immersed boundary conditions for simulation of complex fluid flows, Fluid Dyn. Mater. Process. 7 (3) (2011) 241–258.

[37] R. Tahir-Kheli, Ordinary Differential Equations. [Electronic Resource] : Mathematical Tools for Physicists, Springer International Publishing, 2018.

[38] G. Tryggvason, R. Scardovelli, S. Zaleski, Direct Numerical Simulations of Gas-Liquid Multiphase Flows, Cambridge University Press, 2011.

[39] O. Ubbink, R. Issa, A method for capturing sharp fluid interfaces on arbitrary meshes, J. Comput. Phys. 153 (1) (1999) 26–50, http://dx.doi.org/10.1006/jcph.1999.6276.

[40] M. Niethammer, G. Brenn, H. Marschall, D. Bothe, An extended volume of fluid method and its application to single bubbles rising in a viscoelastic liquid, J. Comput. Phys. 387 (2019) 326–355, http://dx.doi.org/10.1016/j.jcp.2019.02.021, URL http://www.sciencedirect.com/science/article/pii/S002199911930138X.

[41] J. Göhl, A. Mark, S. Sasic, F. Edelvik, An immersed boundary based dynamic contact angle framework for handling complex surfaces of mixed wettabilities, Int. J. Multiph. Flow. 109 (2018) 164–177, http://dx.doi.org/10.1016/j.ijmultiphaseflow.2018.08.001, URL https://www.sciencedirect.com/science/article/pii/S0301932217306444.